5726–5742 *Nucleic Acids Research, 2021, Vol. 49, No. 10* *Published online 22 May 2021*
https://doi.org/10.1093/nar/gkab362

Discordant regulation of eIF2 kinase GCN2 and mTORC1 during nutrient stress

Jagannath Misra[1], Michael J. Holmes[1,2], Emily T. Mirek[3], Michael Langevin[3], Hyeong-Geug Kim[1], Kenneth R. Carlson[1], Malcolm Watford[3], X. Charlie Dong[1,4], Tracy G. Anthony[3,*] and Ronald C. Wek[1,*]

[1]Department of Biochemistry and Molecular Biology, Indiana University School of Medicine, Indianapolis, IN 46202 USA, [2]Department of Pharmacology and Toxicology, Indiana University School of Medicine, Indianapolis, IN 46202 USA, [3]Department of Nutritional Sciences, Rutgers University, New Brunswick, NJ 08901 USA and [4]Department of BioHealth Informatics, School of Informatics and Computing, Indiana University Purdue University Indianapolis, Indianapolis, IN, USA

Received October 11, 2020; Revised April 07, 2021; Editorial Decision April 21, 2021; Accepted April 23, 2021

ABSTRACT

Appropriate regulation of the Integrated stress response (ISR) and mTORC1 signaling are central for cell adaptation to starvation for amino acids. Halofuginone (HF) is a potent inhibitor of aminoacylation of tRNA^{Pro} with broad biomedical applications. Here, we show that in addition to translational control directed by activation of the ISR by general control nonderepressible 2 (GCN2), HF increased free amino acids and directed translation of genes involved in protein biogenesis *via* sustained mTORC1 signaling. Deletion of GCN2 reduced cell survival to HF whereas pharmacological inhibition of mTORC1 afforded protection. HF treatment of mice synchronously activated the GCN2-mediated ISR and mTORC1 in liver whereas *Gcn2-null* mice allowed greater mTORC1 activation to HF, resulting in liver steatosis and cell death. We conclude that HF causes an amino acid imbalance that uniquely activates both GCN2 and mTORC1. Loss of GCN2 during HF creates a disconnect between metabolic state and need, triggering proteostasis collapse.

INTRODUCTION

Cells respond to environmental stress by reprogramming gene expression to alleviate cellular damage and achieve homeostasis. A central mechanism for this reprogramming involves regulation of translation initiation, which rapidly induces expression of stress adaptive proteins and optimizes utilization of nutrients and energy. During the initiation phase of translation, eukaryotic initiation factor 2 (eIF2) combined with GTP escorts initiator tRNA (Met-tRNA$_i^{Met}$) to the P site of ribosomes, facilitating start codon selection. In response to environmental stresses such as amino acid depletion, there is increased phosphorylation of the α-subunit of eIF2 (P-eIF2α), which inhibits the guanine nucleotide exchange factor eIF2B. The eIF2B inhibition by P-eIF2α sharply reduces eIF2-GDP to eIF2-GTP exchange, lowering delivery of Met-tRNA$_i^{Met}$ to ribosomes that culminates in repression of bulk translation (1). Lowered eIF2 recycling also directs preferential translation of select gene transcripts, such as *Atf4*, which encodes a transcriptional activator of genes involved in amino acid synthesis and import, autophagy, and protection from oxidative stress (2–5).

There are multiple eIF2α kinases, each responding to different stress conditions. For example, GCN2 (EIF2AK4) is activated by amino acid depletion by mechanisms suggested to involve GCN2 binding of uncharged tRNAs which accumulate during starvation of their cognate amino acids (6,7). Furthermore, stalling and collisions of elongating ribosomes are reported to activate GCN2 during certain stresses by a signaling pathway suggested to involve ZAK protein kinase (8–11). Other members of the eIF2α kinase family include HRI (EIF2AK1), induced by heme and iron depletion in erythroid cells and by mitochondrial stress (12–14), and PERK (EIF2AK3) and PKR (EIF2AK2), which are activated by endoplasmic reticulum (ER) stress and viral infection, respectively (1,15,16). Because P-eIF2α is induced by multiple cellular stresses to direct global and gene-specific translation, this pathway is referred to as the Integrated stress response (ISR) (17).

In addition to the ISR, the mechanistic target of rapamycin complex 1 (mTORC1) signaling pathway also regulates translational control and cell growth in response to changes in availability of amino acids, growth factors, and energy (18). Many target proteins are phosphorylated by

*To whom correspondence should be addressed. Tel: +1 317 274 0549; Email: rwek@iu.edu
Correspondence may also be addressed to Tracy G. Anthony. Tel: +1 848 932 6331; Email: tracy.anthony@rutgers.edu

mTORC1, which collectively enhance ribosome biogenesis and translation initiation (18,19). Abundant levels of certain amino acids serve to increase mTORC1 phosphorylation of LARP1, which increases eIF4F assembly on 5′-TOP mRNAs (20,21). Simultaneously, mTORC1 phosphorylation of 4EBPs allows for the recruitment of preinitiation complex to 5′-TOP mRNAs for translation initiation (22).

Dysregulation of nutrient sensing can lead to inappropriate or uncontrolled mRNA translation, disrupting proteostasis and harming cellular integrity (1,6,23). GCN2 is activated by amino acid starvation, whereas starvation for certain amino acids, such as leucine, methionine and arginine, repress mTORC1. We previously reported that mTORC1 repression is abrogated in *Gcn2-null* mice fed a leucine-devoid diet (24) or treated with asparaginase (25), indicating that these signaling pathways are coordinated in response to diet and drug-mediated forms of amino acid deprivation. Discordant regulation between the ISR and mTORC1 signaling is also reported in tuberous sclerosis complex-deficient cells, leading to enhanced protein synthesis that overwhelms the processing capacity of the secretory pathway and creates ER stress that can culminate in cell death (26). These observations emphasize that proper reciprocal regulation between the ISR and mTORC1 is a prerequisite for protein homeostasis and cell survival.

Here, we show that treatment with halofuginone (HF), a small molecule inhibitor of glutamyl-prolyl-tRNA synthetase (EPRS) (27), induces ISR-directed translational control by mimicking amino acid depletion via enhanced uncharged tRNAs that activate GCN2. Of interest, HF also increases free amino acids and supports sustained mTORC1 activity. The concurrent ISR and mTORC1 activities adversely affects cell viability, which could be alleviated in part by pharmacological repression of mTORC1. Furthermore, *Gcn2-null* mice fail to suppress mTORC1 during HF exposure, corresponding with greater hepatotoxicity as compared to wild type mice. This investigation illustrates that proteostasis control during amino acid stress requires proper coordination between the GCN2 and mTORC1 pathways.

MATERIALS AND METHODS

Cell Culture and treatment regimens

WT and *Gcn2*$^{-/-}$ MEF cells were cultured in DMEM supplemented with 10% FBS as previously described (28). Human hepatoma cells (HepG2) were maintained in MEM as previously described (29). For all HF treatments, first cells were seeded in plates with 10% normal FBS containing media, 6 h later existing media was replaced with 10% dialyzed FBS containing media (to minimize the presence of proline in the media). After culturing the cells for 18–20 h, the indicated concentrations HF were added for the indicated times. For histidinol treatment, MEF cells were seeded in plates with DMEM supplemented with 10% FBS. After 6 h, the media was replaced with DMEM supplemented with 10% dialyzed FBS to minimize the presence of histidine in the media and after culturing for 18–20 h the cells were treated with 2 mM histidinol for 6 h. To induce ER stress, MEF cells were treated with 2 μM tunicamycin for 6 h.

Animals

Animal protocols were approved by the Institutional Animal Care and Use Committees at Rutgers University. Adult (15–25 weeks old) wild type (WT) and *Gcn2*$^{-/-}$ mice ($n = 4$ per group; consisting of two males and two females) both on the C57BL/6J genetic background were used in these experiments. Animals were administered once daily IP injections of either 0.5 mg/kg HF or 0.5% DMSO as vehicle. One group received a single injection and was euthanized 8 h later. The other group received one injection, then a second injection 24 h later, and was euthanized 24–44 h after the first injection. Animals were euthanized by decapitation and tissues were flash frozen in liquid nitrogen.

Immunoblot analyses

Whole cell extracts were prepared in 1% SDS solution containing protease inhibitors. Equal amounts of proteins from the cell lysates were separated by SDS-PAGE, followed by immunoblot analyses as previously described (28). Proteins bound to membrane filters were probed with the specified antibodies and immunoreactive proteins were visualized using chemiluminiscence using either X-ray film or the Bio-Rad Chemidoc MP imaging system. Antibodies using in the immunoblot analyses include the following: P-GCN2 (Abcam, #Ab75836), total GCN2 (Abcam, #ab137543), P-eIF2α (Abcam, #ab32157), total eIF2α (Cell Signaling Technology, #5324S), ATF4 antibody was prepared against the corresponding recombinant human proteins, which were affinity purified (30), P-mTOR (Cell Signaling Technology, #2971S), total mTOR (Cell Signaling Technology, #2983S), P-S6K1 (Cell Signaling Technology, #9205S), total S6K1 (Cell Signaling Technology, #9202S), *P*-4EBP1 (Cell Signaling Technology, #2855S), total 4EBP1 (Cell Signaling Technology, #9644S), PRODH (Proteintech, # 22980-1-AP) and β-actin (Sigma, #A5441). Quantification of immunoblots was carried out by measuring relative band intensities measured using ImageJ software, which was normalized as indicated.

tRNA charging assays

Total and uncharged tRNA levels were measured similar to that previously described (31,32). In this method, RNA was extracted from cells using TRIzol (Life Technologies, 15596018). RNA was then treated with either 12.5 mM $NaIO_4$ (oxidized) or 12.5 mM NaCl (unoxidized) in sodium acetate buffer (pH 4.5) in the dark at room temperature for 20 min followed by quenching with 0.3 M glucose. All mature tRNA ends with 3′-CCA. $NaIO_4$ will only oxidize the of 3′-A residue of uncharged tRNAs since the 3′ end of charged tRNAs are protected by amino acids; a parallel mock treatment with NaCl was carried out which resulted in no oxidation for tRNAs. The tRNA samples were then spiked with 7.3 ng yeast $tRNA^{Phe}$ (R4018, Sigma) for internal normalization, followed by desalination through MicroSpin G-50 column (27533001, GE Healthcare). Next, tRNA was discharged (deacylation through β-elimination) in a solution of 50 mM Tris–HCl (pH 9.0) at 37°C for 45 min. Following

deacylation, 5′-adenylated adaptor (5′-/5rApp/TGGAATTCTCGGGTGCCAAGG/3ddC/-3′) was ligated to the tRNAs using T4 RNA ligase2 truncated KQ (M0351L, New England BioLabs). The 5′-adenylated adaptor cannot be ligated to the uncharged tRNAs in samples which were treated with $NaIO_4$. This is because following oxidation, β-elimination in the basic condition selectively removed the oxidized 3′-A residue, leaving a 3′-phosphate at the terminal 3′-C residue for uncharged tRNAs, whereas β-elimination removes the amino acid attached to the 3′-A residue of charged tRNAs, resulting in 3′-A-OH for these charged tRNAs. The presence of 3′-phosphate at the terminal 3′-C blocked uncharged tRNAs from being ligated to the 5′-adenylated adaptor for downstream processing in samples treated with $NaIO_4$. Next An oligo (5′-GCCTTGGCACCCGAGAATTCCA-3′), complementary to the adaptor sequence, was used for cDNA synthesis using SuperScript IV RT kit (Invitrogen, 18090050). cDNA was used for qPCR based detection of tRNAs with the following primers: yeast $tRNA^{Phe}$ fw-GCGGAYTTAGCTCAGTTGGGAGAG, rev-GAGAATTCCATGGTGCGAAYTCTGTGG; mouse $tRNA^{Pro}$ fw-GGCTCGTTGGTCTAGGGGTA, rev-GAGAATTCCATGGGGGCTCGTCC; mouse $tRNA^{Asn}$ fw-GTCTCTGTGGCGCAATCGGT, rev-GAGAATTCCATGGCGTCCCT GG. In $NaIO_4$ treated samples, only charged tRNAs were amplified by the qPCR whereas for NaCl treated samples both charged and uncharged tRNAs were amplified. Results were first normalized to the spiked yeast $tRNA^{Phe}$, uncharged tRNA fractions were then calculated by subtracting the charged fraction of tRNAs ($NaIO_4$ treated) from total tRNAs (NaCl treated).

Polysome profiling

MEF cells were treated with either 2 μM tunicamycin or 100 nM HF for 6 h or left untreated. Cycloheximide was added to each culture dish at a final concentration of 50 μg/ml for 10 min before harvesting. Cells were rinsed with ice-cold PBS solution containing 50 μg/ml cycloheximide and then lysed with 500 μl of cold lysis solution containing 20 mM Tris·HCl (pH 7.5), 100 mM NaCl, 10 mM $MgCl_2$, 0.4% NP-40, and 50 μg/ml cycloheximide, followed by centrifugation at 15 871 × g for 10 min at 4°C. Cell lysates were then applied to the top of 10–50% sucrose gradients and subjected to ultracentrifugation in a Beckman SW41Ti rotor at 40 000 rpm for 2 h at 4°C. A piston gradient fractionator (BioComp) and a 254 nm UV monitor with Data Quest Software were used to generate whole cell lysate polysome profiles as described previously (33).

Ribo-Seq analyses

Samples for ribosome profiling were prepared as previously described (34). Briefly, cell lysates were prepared using the lysis solution described for polysome preparations, which was supplemented with 25 units/ml of Turbo DNase I (Invitrogen). A small portion of cell lysate was immediately stored in TRIzol LS reagent (Ambion) for total RNA isolation. The remaining portion of the cell lysate was digested with 100 units of RNase I (Ambion) at 4°C for 1 h with mild agitation. Sample digestion was quenched by adding 200 units of SUPERase·IN (Ambion). Digested samples were then placed on top of 10–50% sucrose gradients supplemented with SUPERase·IN and subjected to ultracentrifugation in a Beckman SW41Ti rotor at 40 000 rpm for 2 h at 4°C. Following centrifugation, the fractions corresponding to the monosome peak of the digested samples were collected using a Biocomp piston gradient fractionator coupled with a Gilson fraction collector and stored in TRIzol LS reagent. RPFs and total RNA were collected using TRIzol reagent. Total RNA was fragmented by alkaline hydrolysis. RPFs and fragmented RNA were collected by gel extraction from a 15% denaturing TBE-urea gel (Invitrogen) and processed for library preparation as previously described (34). Ribo-minus kit (Ambion, A15017) was used to deplete rRNA. Paired-end 150-bp reads were generated on a HiSeq system (Illumina).

Sequencing reads were processed with the FASTX toolkit and reads aligning to rRNA and tRNA were removed in silico with bowtie (35). The remaining reads were mapped with HISAT2 (36) to the GRCm38 genome assembly, assigned to annotated genomic features with htseq-count (37), and differential expression was assessed with DESeq2 (38). Analysis of translationally controlled genes was conducted with RiboRex (39). Enrichment analyses were obtained with GOseq (40) and Ingenuity Pathway Analysis (41). Ribosome protected fragments were filtered by length then mapped to the corresponding regions of gene transcripts using the RiboWaltz package in R with ENSMBL GRCm38 annotations. RiboWaltz was also used to identify the P-site and A-site codons for each RPF, this information was then used to calculate the A-site occupancy for each codon. The A-site occupancy for each amino acid was calculated by summing the occupancies for each codon within each amino acid, and a pooled standard deviation was calculated for each amino acid occupancy by taking the square root of the sum of squares of the standard deviation for each codon within that amino acid. These derived A-site occupancies and pooled standard deviations for each amino acid were used in a Welch's *t*-test to identify differential occupancy upon HF treatment. To account for multiple hypothesis testing in determining differential A-site occupancy, Benjamini-Hochberg FDR correction was applied to the *P*-value output of the Welch's t-test and statistical significance was determined by applying an FDR corrected *P*-value cutoff of 0.1. All data sets from this study are available in the NCBI GEO database (accession no. GSE156850).

Amino acid measurements

Cellular amino acids levels were measured as previously described (42). Briefly, cell pellets were resuspended in a solution of 0.1% formic acid in methanol and briefly vortexed for about 5 seconds. Cells were then lysed by three cycles of freezing in liquid nitrogen (LN2) for 3 min and thawing at 42°C for 10 min. Cell lysates were prepared and clarified and analyzed by reverse-phase liquid chromatography with appropriate standard curves for amino acids as previously described (42).

MTT assays

WT and *Gcn2*$^{-/-}$ MEF cells were seeded in 96-well culture plates at 5000 cells/well. The following day, cells were treated with 50 or 100 nM HF for 6 h in the presence or absence of 25 nM Torin1. The treated cells were then allowed to recover in fresh medium for 18 h. Cell viability was assessed through the conversion of tetrazolium (MTT) to formazan by measuring the absorbance at 570 nm using CellTiter 96-well nonradioactive cell proliferation assay (Promega, #G4000). Absorbance values were normalized to WT non-treated cells and presented as cell viability.

Serum biochemistry and hepatic lipid analyses

Serum alanine aminotransferase (ALT) levels were measured using the Pointe Scientific ALT (SGPT) reagent set according to the manufacture's manuals. For hepatic triglycerides (TG), hepatic lipids were extracted as previously described (43), and analyzed using the WACO L-type triglyceride M assay kit (Fugifilm WACO diagnostics, # 994-02891, # 990-02991) following the manufacture's protocol.

Histopathology and immunohistochemistry (IHC) analyses

Liver tissues were fixed in a 10% neutral formalin solution and processed for paraffin embedding and sectioning at the Histology Core of Indiana University School of Medicine. Hematoxylin and eosin (H&E) stain were performed following standard protocols (4 μm thickness). Quantitative scoring of H&E-stain was carried out double blinded as previously described (44,45). Briefly, each section was evaluated for hepatic steatosis and inflammation scores using grades of '0' to '4' based on the average percent of fat-accumulated hepatocyte per field at 200× magnification under H&E staining. Grade 0 indicates <5% of fat accumulation; grade 1, 5–25% of fat accumulation; grade 2, 26–50% of fat accumulation; grade 3, 51–75% of fat accumulation; grade 4, >75% of fat accumulation).

IHC analyses were carried out to measure cleaved-caspase-3, p-MLKL, 4-HNE and nitrotryptophan. Sections of liver tissues were deparaffinized, hydrated, and then heated in sodium citrate buffer for antigen retrieval at 100 °C for 5 min. Samples were then treated with normal horse serum (2.5%) for 1 h and the sections were incubated with antibodies against Cleaved Caspase-3 (Asp175) (1:200, Cell Signaling Technology, #9664), phospho-MLKL (Ser345) (D6E3G) (1:200, Cell Signaling Technology, #37333), 4-HNE (1:250, R&D system, #MAB3249), Nitrotryptophan (1:50, Thermo Scientific, #2D12) for overnight. After washing with PBS solution containing 0.05% Tween-20, tissue sections were incubated with a biotinylated universal pan-specific antibody (PK-7200, Vectastain ABC kit, Vector Laboratories, Burlingame, CA) for 2 h. Tissue sections were exposed to an avidin-biotin peroxidase complex (Vector Laboratories) for 1 h and peroxidase activity was visualized using a stable diaminobenzidine solution (Vector Laboratories). Images were captured by microscopy (100 to 400× magnification, Leica, Germany).

TUNEL assays

TUNEL apoptosis was measured by ApopTag® Peroxidase In Situ Apoptosis Detection Kit (Millipore, #S7100). Briefly, liver tissues were fixed in 10% formalin and embedded with paraffin. After deparaffinization and washing, liver tissue samples were incubated with 2 μg/ml proteinase k at room temperature for 15 min and then 3% hydrogen peroxide was applied to quench the peroxidase. Following several washing steps, the liver tissue sections (4 μm of thickness) were incubated with terminal deoxynucleotidyl transferase (TdT) at 37°C for 90 min. Next the slides were washed using running tap water, and treated with anti-digoxigenin-peroxidase for 1 h at room temperature. The slides were then washed, signals were detected by a stable chromogen, 3,3′-diaminobenzidine (DAB) followed by washing. After observing the positive signals, hematoxylin counter staining was performed. Representative images of TUNEL were obtained by microscopy (100–400× magnification, Leica, Germany). Quantification analyses from the final stained slide were performed by counting randomly chosen positive signals in a double-blind manner (total four randomly chosen areas per section, $n = 4$ per group).

Hepatic oxidation analyses

Liver tissue was homogenized in a 1% SDS solution containing protease inhibitor. Hepatic NO levels were measured using the Nitric Oxide Assay Kit (Colorimetric, Abcam, Cambridge, UK, #ab65328), and hepatic intracellular H_2O_2 levels were determined using the Amplex™ Red Hydrogen Peroxide/Peroxidase Assay Kit (Thermo Fisher Scientific, #A22188).

Statistical analyses

Two-tailed Student's t-tests were used to calculate statistical significance. P values <0.05 were considered statistically significant and are indicated by asterisks. Data are expressed as the means ± SD and are representative of at least three independent experiments.

RESULTS

HF is a febrifugine derivative that was previously identified as an inhibitor of prolyl tRNA synthetase activity of the enzyme EPRS that lowers $tRNA^{Pro}$ charging to activate GCN2 in the ISR (27). To further address the mechanisms by which HF activates the ISR and directs translational control, mouse embryonic fibroblast (MEF) cells (Figure 1A, left panel) and human hepatoma cells (HepG2) (Figure 1A right panel) were treated with increasing concentrations of HF. In both cell lines, increasing doses of HF enhanced the levels of P-eIF2α and phosphorylation of GCN2 (P-GCN2), a measure of activation of GCN2, as judged by immunoblot analyses. Furthermore, HF increased ATF4 protein expression, whose translation is induced by P-eIF2α (2–4). Of interest, while P-eIF2α continued to be elevated with increased concentrations of HF, ATF4 protein levels were maximal at 100 and 50 nM HF in MEF cells and HepG2 cultures, respectively (Figure 1A). At higher concentrations of HF, the amount of ATF4 was

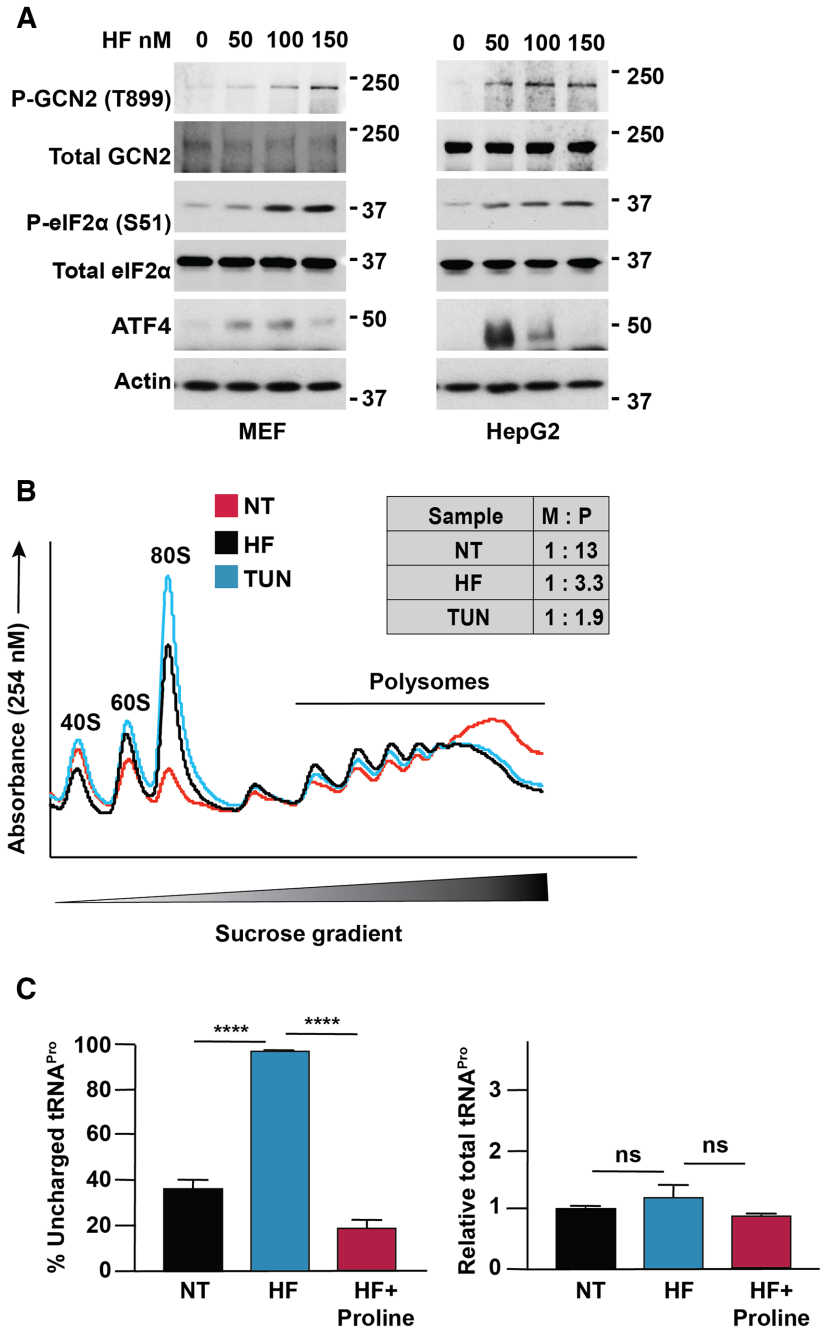

Figure 1. HF lowers charging of $tRNA^{Pro}$ and induces GCN2 and translational control. (**A**) MEF cells (left panel) and HepG2 cells (right panel) were treated with HF at the designated concentrations for 6 h and levels of the indicated proteins were measured by immunoblot analyses using specific antibodies. In parallel, levels of phosphorylation of GCN2 and eIF2α were measured by immunoblot. (**B**) MEF cells were treated with 100 nM HF or 2 μM tunicamycin (TUN) for 6 h or left untreated (NT). Cells were collected, lysed, and separated by centrifugation in a sucrose gradient. Gradients were fractionated with monitored at absorbance of 254 nm. Free 40S and 60S ribosomes, 80S monosomes, and large polysomes are indicated. Relative amounts of monosomes (M) and large polysomes (P) are presented. (**C**) MEF cells were treated with 100 nM HF alone or along with 3 mM proline for 6 h, or left untreated (NT). The percentage of uncharged $tRNA^{Pro}$ (left panel) and relative amounts of total $tRNA^{Pro}$ (right panel) were measured by a RT-qPCR as described in the materials and methods. Significant differences between treatments are indicated. $^{****}P < 0.0001$; ns, not significant.

reduced. These results suggest that there are optimal levels of HF-directed uncharged $tRNA^{Pro}$ and accompanying increased P-eIF2α for peak ATF4 expression. Increasing concentrations of HF can severely deplete aminoacylated $tRNA^{Pro}$ needed for efficient translation elongation, thus lowering amounts of ATF4 protein expression despite robust P-eIF2α.

Induction of P-eIF2α is a potent repressor of bulk translation initiation. There were reductions of large polysomes accompanied by accumulation of monosomes, which is diagnostic of lowered initiation of protein synthesis, in response to incubation of MEF cells with either HF or tunicamycin, a well-documented inducer of ER stress and the related eIF2α kinase PERK (Figure 1B). Next we addressed whether HF increased uncharged $tRNA^{Pro}$ levels since it is a competitive inhibitor of the prolyl-tRNA synthetase activity of EPRS (27). HF treatment of MEF cells significantly increased uncharged $tRNA^{Pro}$ levels and the inhibition of aminoacylation of $tRNA^{Pro}$ was reversed by the addition of proline (Figure 1C). There were no appreciable differences in the amounts of total $tRNA^{Pro}$ in response to HF exposure (Figure 1C) and there were no significant changes in charging of $tRNA^{Asn}$, emphasizing the specificity of the HF for the EPRS (Supplementary Figure S1). These results indicate that HF triggers increased levels of uncharged $tRNA^{Pro}$, leading to enhanced P-eIF2α by GCN2 and lowered global translation initiation accompanied by preferential expression of the ISR core effector, ATF4.

Ribosomal profiling reveals ribosome pausing at proline codons and discordant regulation of eIF2 and mTORC1 signaling during HF treatment

To determine the effect of HF on the transcriptome and mRNA translation, we carried out Ribo-Seq and RNA-Seq analyses of MEF cells that were treated with 100 nM HF for 6 h (Figure 2A). To ensure that the ISR was appropriately induced by HF, increased amounts of P-eIF2α and ATF4 were confirmed in parallel with the cell preparations (Supplementary Figure S2A, B). Mapping of the ribosome protected footprints (RPFs) to the corresponding regions of mRNA showed that ribosomes were highly enriched to the coding sequences (CDS) (Figure 2B). The RPFs displayed a strong trinucleotide periodicity that was in frame with annotated CDS, a characteristic of translating ribosomes (Figure 2C and Supplementary Figure S2C). Consistent with reduced $tRNA^{Pro}$ charging in response to HF exposure, the fractional ribosomal A-site occupancy for proline was significantly increased for three of the four proline codons (CCC, CCG and CCT) (Figure 2D and Supplementary Figure S2D). There was also increased occupancy for the fourth proline codon, CCA, although it did not reach significance (Supplementary Figure S2D). These results indicate that HF causes pausing of translating ribosomes at proline codons at the A-site of ribosomes and this is likely to also contribute to the decreased levels of protein synthesis.

Exposure to HF caused changes in the transcriptome and translatome (Figure 3A and Supplementary Table S1). Six hundred and forty-six genes showed concordant changes in both mRNA levels and ribosome occupancy (in red, RNA + RPF), suggesting that these genes were regulated primarily at the mRNA level. These transcripts displayed a change in RPF density that was proportional to their change in mRNA abundance, indicating that the mRNAs maintained a similar level of translation efficiency upon exposure to HF. Approximately 1500 genes (in yellow and green) displayed discordance between their mRNA abundance and ribosome density, suggesting that these transcripts were also subjected to translation control (Figure 3A). For example, genes that show a decreased RPF density below the changes seen in mRNA abundance, as delineated by the right-hand yellow and lower green populations, were likely translationally repressed upon HF exposure. In contrast, genes in the left-hand yellow and upper green populations displayed increased RPF density above the changes seen in their transcript abundance, indicating an increase in their translational efficiency (Figure 3A).

We ranked the genes that were differentially expressed at both the mRNA and RPF levels (FDR$\leq$ 0.05) based on their $\log_2$FC values and determined that there was a high degree of correlation between mRNA steady-state and ribosome density (Figure 3B). As expected, while the amount of the *Atf4* transcript was modestly increased in response to HF, there was a large increase in its ribosome density, indicative of HF-induced preferential translation (Figure 3B, C and Supplementary Table S2). Furthermore, *Chop* (*Ddit3*) and *Gadd34* (*Ppp1r15A*) genes were also induced at the both transcript and translational levels (Figure 3B, Supplementary Table S1), which is consistent with prior reports of their regulation by the ISR (4,46–50). *Gadd34* and *Chop* were counted among the preferentially translated genes although the latter missed the FDR cutoff by a small margin ($q = 0.054$) (Supplementary Table S2). Together, these analyses show that HF induces the production of key effectors in the canonical ISR network.

We conducted gene ontology (GO) analyses (40) of the differentially-expressed mRNAs and RPFs to determine the molecular functions that were altered following incubation with HF. There was a high degree of overlap in the upregulated GO terms derived from both lists of differentially-expressed mRNAs and RPFs (Supplementary Table S3). Top shared GO terms included DNA binding, histone binding, and transcription factor activity, implying that a transcriptional remodeling occurs upon HF exposure. Ingenuity Pathway Analysis (IPA) (41) of our datasets pointed to an increase in cell growth and replication, functions typically associated with increased metabolic throughput and translational activation (Figure 3D). These results were surprising because HF triggers the ISR (Figure 1), which in turn dampens bulk translation and curtails cell division to facilitate adaptation to the cellular stress. We therefore further mined our data for evidence of translationally controlled gene expression during HF stress.

Of importance, the list of preferentially translated genes was strongly enriched for ribosomal proteins (Figure 3C and E and Supplementary Table S4), which are encoded by mRNAs with 5′-leaders containing terminal oligopyrimidine tract (TOP) (22,51,52). These 5′-TOP containing gene transcripts are translationally induced by the activation of mTORC1 (51). Indeed, IPA of the genes subject to translational control revealed that both the eIF2 and mTOR sig-

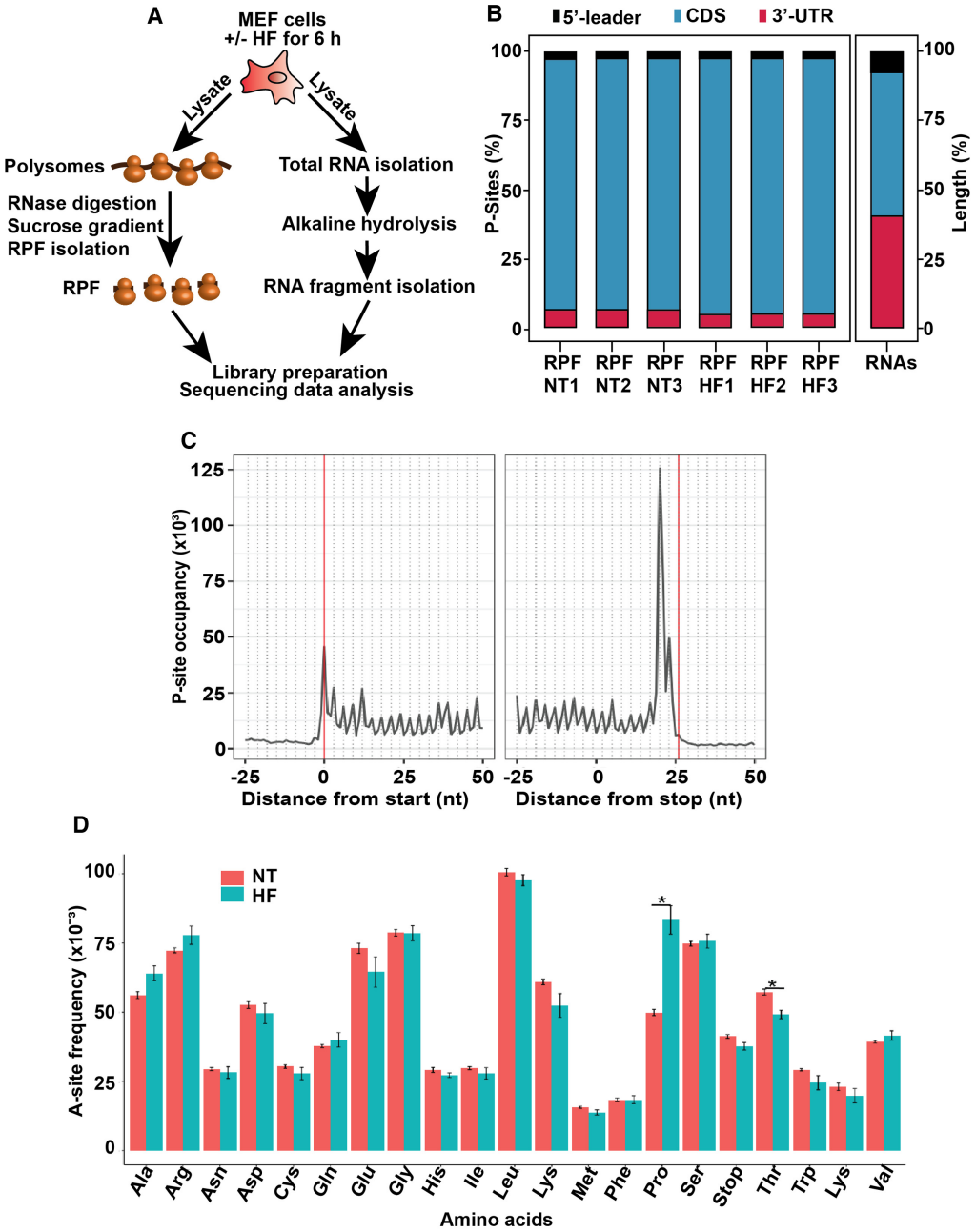

Figure 2. Ribo-seq analyses reveals ribosome pausing at proline codons. (**A**) Schematic for design of Ribo-Seq and RNA-Seq analyses. MEF cells were treated with 100 nM HF for 6 h or left untreated (NT). Cell lysate was divided in two parts for Ribo-Seq and RNA-Seq analyses. For Ribo-Seq, lysates were first digested with RNase I and then separated by sucrose gradient centrifugation. Monosomes were collected by polysome profiling analysis. Ribosome protected footprints (RPFs) were collected for sequencing library preparation. For RNA-Seq, total RNA was isolated from cell lysates, followed by alkaline hydrolysis to generate smaller fragments that were processed for sequencing library preparation. (**B**) Bar plot displaying the fraction of RPFs from untreated (NT) or HF treated cells that map to the 5′-leader, CDS, and 3′-UTR for each ribosome profiling sample. Each RPF was mapped onto the corresponding region of mRNA using the RiboWaltz package in R with ENSMBL GRCm38 annotations, and the fraction of RPFs in each of these regions was graphed. The rightmost panel depicts the expected distribution of reads in a random sampling of total RNA. As expected, each of the Ribo-Seq were enriched for the CDS regions of the gene transcripts. (**C**) Metaprofile showing the location of each ribosome footprint P-site in relation to translation start and stop sites across all gene transcripts. For each ribosome footprints, the trinucleotide present at the ribosome P-sites were identified and the distance from either the translation start or stop sites were mapped for all transcripts using the RiboWaltz package in R. A trinucleotide periodicity was observed that is characteristic of translating ribosomes in the CDS of transcripts, but not upstream of the translation start site or downstream of the termination site. (**D**) Bar plot displaying the fractional occupancy of codons for each amino acid. The ribosome A-site occupancy of all codons was pooled for each amino acid and the relative amounts were represented in cells treated with HF or left untreated (NT). The y-axis represents the proportion of A-sites occupied by each amino acid; it is calculated by dividing the number of A-site reads for each amino acid by the total number of A-sites. Error bars represent the pooled standard deviation for all codons within each amino acid and asterisks indicate statistical significance as determined by Benjamini-Hochberg FDR correction with a *P*-value cutoff of 0.1 after performing a Welch's t-test. For threonine and proline, Welch's *t*-test produced *P*-values of 0.0027 and 0.0059 which correspond to FDR adjusted *P*-values (P-adj.) of 0.057 and 0.0619 respectively. Significant differences between treatments are indicated. *, FDR *P*-adj. < 0.1.

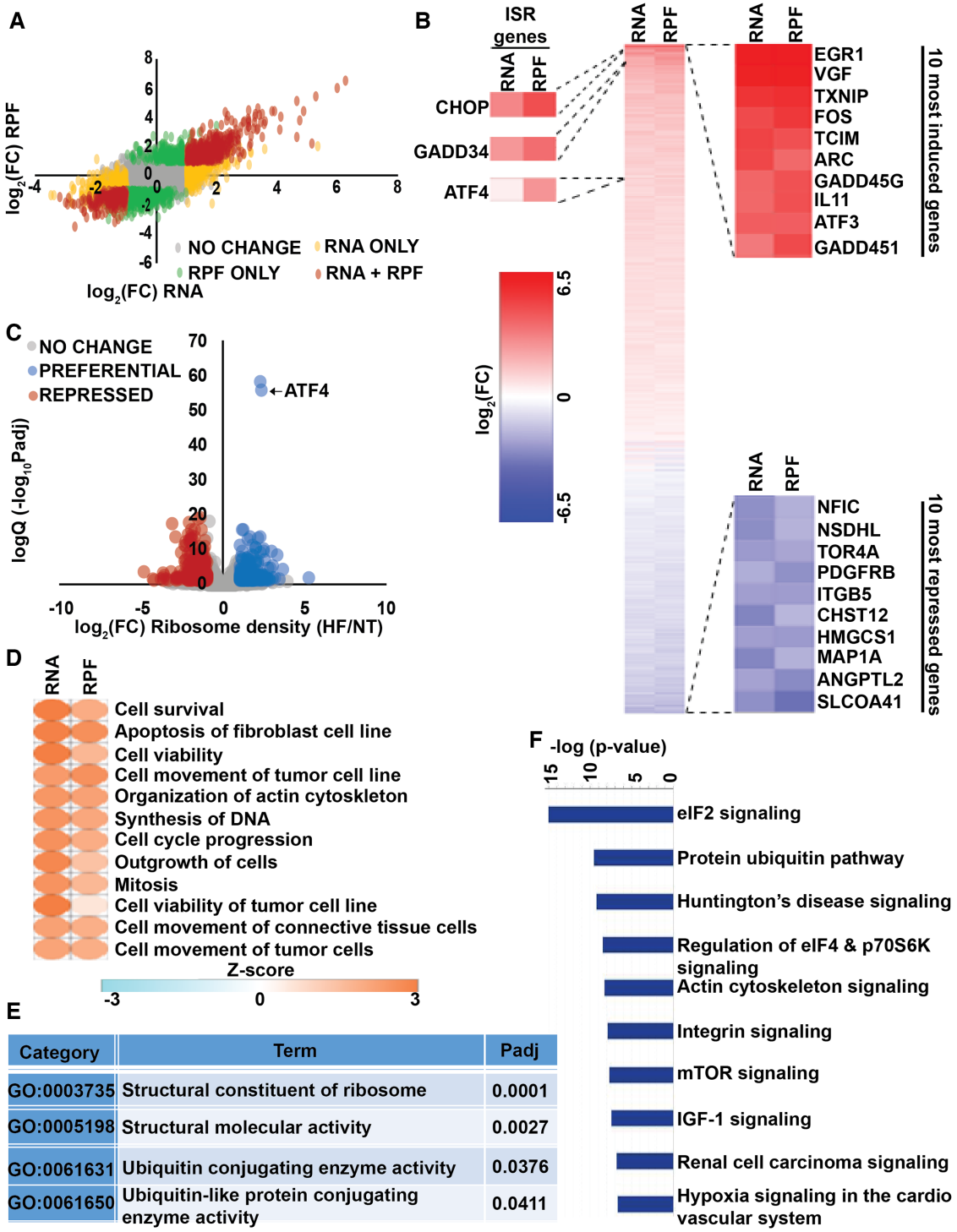

E

Category	Term	Padj
GO:0003735	Structural constituent of ribosome	0.0001
GO:0005198	Structural molecular activity	0.0027
GO:0061631	Ubiquitin conjugating enzyme activity	0.0376
GO:0061650	Ubiquitin-like protein conjugating enzyme activity	0.0411

Figure 3. Discordant regulation of the ISR and mTORC1 signaling during HF treatment. (**A**) Scatterplots of log2 fold changes of mRNA steady-state (RNA) and RPF libraries for MEFs treated with 100 nM HF for 6 h. Colored genes are those that are differentially represented with an adjusted *P* value (Benjamini-Hochberg method) that meets a false-discovery rate (FDR) of ≤0.01. Red dots represent genes that change in mRNA and RPF abundance, yellow dots represent genes that change in mRNA abundance only, and green dots represent genes that change in RPF abundance only. (**B**) Heat map of all differentially expressed genes with a p-adj value of ≤ 0.01 identified in ribosome profiling (RPF) and RNA-seq (RNA) data sets for MEF cells upon 100 nM HF treatment for 6 h. Rows are ordered from most induced (red) to most repressed (blue). The top 10 genes from each extreme are presented. (**C**) Volcano plot of ribosome density (translational efficiency) for MEFs treated with 100 nM HF for 6 h. Significantly (FDR ≤ 0.05) preferentially translated genes are in blue, significantly translationally repressed genes are in red. (**D**) Ingenuity Pathway Analysis (IPA) of modulated canonical pathways in MEFs upon 100 nM HF treatment for 6 h. Top 10 enriched pathways with a *P*-adj value of ≤0.05 are presented. (**E**) Gene ontology enrichment analysis of molecular functions associated with genes that displayed increased ribosome density, indicative of enhanced translational efficiency, in response to 100 nM HF treatment for 6 h. (**F**) IPA of modulated cellular and molecular functions in MEFs upon 100 nM HF treatment for 6 h. Pathways with a significance of a *P* value of ≤0.05 and that displayed a *Z* score ±2 in either the RPF or RNA data sets are shown.

naling pathways were impacted, which was intriguing since the former represses bulk translation whereas the later promotes it (Figure 3F). Together, the observed increase in progrowth associated gene expression, apparent involvement of genes associated with mTOR signaling, and the observed increase in translation of ribosomal proteins, and we therefore elected to determine how mTORC1 signaling was affected by HF exposure.

HF elevates intracellular amino acids and supports mTORC1 signaling

The genome-wide analyses of gene expression suggested that there was elevated mTORC1 signaling in HF-treated cells. To further evaluate the effects of HF on mTORC1 signaling, we used immunoblot analyses to measure phosphorylation of mTORC1 and its downstream targets 4EBP1 and S6 kinase 1 (S6K1) in MEF cells treated with HF for 6 h. There were high levels of phosphorylation of each of these proteins independent of treatment group (Figure 4A and B), with phosphorylation of S6K1 showing a significant increase upon HF treatment. These results further support the idea that mTORC1 remained active in cells subjected to HF. Addition of Torin1, which is an inhibitor of mTOR (53), sharply reduced mTORC1 activation as judged by the phosphorylation levels of these proteins (Figure 4A and B). By contrast, phosphorylation of GCN2 and eIF2α were low in growing cells and robustly induced upon HF exposure (Figure 4A and B).

Free amino acids, including leucine, methionine, and arginine, function as activators of the mTORC1 pathway (23,54); therefore we measured the levels of free amino acids in the MEF cells incubated with HF (Figure 4C). With the exception of asparagine and tryptophan, each of the measured free amino acids were significantly increased upon HF exposure. Glutamate, glutamine, aspartate, alanine, threonine, and proline, a cognate amino acid for EPRS, were all substantially increased in response to HF (Figure 4C). Notably, glutamate, which can be derived from proline catabolism (55), was highest in intracellular concentrations among all measured amino acids upon HF administration. Furthermore, given that EPRS is a bifunctional aminoacyl tRNA synthetase, enhanced levels of glutamate may also be a consequence of HF indirectly affecting glutamyl tRNA synthetase function of EPRS. These results suggest that inhibition of $tRNA^{Pro}$ charging lowered global translation by lowered eIF2-GTP levels via induced P-eIF2α and by triggered elongation pausing, which together allowed free amino acids to accumulate and support sustained mTORC1 activity.

To address whether lowered tRNA charging involving another amino acid also triggered discordant regulation of GCN2 and mTORC1, we treated MEF cells with histidinol, a structural analog of histidine that blocks charging of $tRNA^{His}$ (56). As expected, histidinol significantly increased the uncharged $tRNA^{His}$ levels (Supplementary Figure S3A) and enhanced P-eIF2α and P-GCN2 (Figure 4D and E). Furthermore, there was a clear trend of increased levels of free amino acid in response to histidinol treatment of MEF cells (Supplementary Figure S3B). Of importance, there were high levels of phosphorylation of S6K1 and 4EBP1 in both non treated and histidinol exposed cells, which were sharply reduced with addition of Torin1 (Figure 4D and E); in fact, phosphorylated S6K1 was increased with histidinol treatment and 4EBP1 trended higher with histidinol although it did not achieve significance (Figure 4E). These results support the idea that mTORC1 is active in cells subjected to different inhibitors of tRNA charging.

Loss of GCN2 and the discordant ISR and mTORC1 regulation reduces cell survival in response to HF

GCN2 has a primary adaptive function in response to cellular stress. To determine the contributions of GCN2 in promoting resilience to HF, we incubated wild-type (WT) and *Gcn2*-deleted MEF cells with 50 nM or 100 nM HF for 6 h, followed by recovery in fresh media for 18 h. Cell viability, as measured by the MTT assay, was progressively lowered in WT cells, with 73% and 40% viable cells measured at 50 nM and 100 nm HF, respectively (Figure 4F). Cell viability was further reduced in cells lacking *Gcn2*, with only 18% of viable cells at 100 nM HF. In parallel, we also assayed the HF-treated WT and *Gcn2*-deleted cells in the presence 25 nM Torin1. Torin1 provided moderate yet significant, resistance to HF in both the WT and *Gcn2*-deleted cells (Figure 4F). These results support the idea that genetic loss of *Gcn2* renders cells more vulnerable to HF and blocking mTORC1 signaling during activation of the ISR by HF improves cell viability.

The ISR and mTORC1 are activated in livers of mice administered HF

To address the effect of HF on the ISR and mTORC1 signaling *in vivo,* WT and whole body *Gcn2-null* mice were administered HF or excipient once daily for 1 day or 2 days and blood and livers were collected 8 h after the first injection or 20 h after the second injection (i.e. 44 h after the first injection). At both times points, there was enhanced hepatic P-eIF2α by HF that was much reduced in the *Gcn2-null* mice (Figure 5A). As expected, there was no measurable GCN2 protein in the *Gcn2-null* mice; therefore, the modest HF induction of P-eIF2α in the *Gcn2-null* liver samples likely reflects another eIF2α kinase, such as PERK as we previously documented (57,58). HF increased P-GCN2 and ATF4 in the livers of WT mice, with liver samples collected at 44 h showing the greatest increases in these ISR biomarkers (Figure 5A). HF supported mTORC1 signaling in the livers of WT mice and phosphorylation levels of mTOR and its downstream target S6 kinase1 (S6K1) were increased even higher in the livers of *Gcn2-null* mice treated with HF for 8 h (Figure 5A); hepatic mTORC1 signaling remained moderately elevated in WT livers by HF at 44 h, with minimal S6K1 phosphorylation in the $Gcn2^{-/-}$ mice.

The interorgan exchange of amino acids contributes importantly to plasma amino acid homeostasis and as such, circulating amino acid concentrations reflect systems-level changes in AA flux and balance (59). In WT mice, most circulating amino acids were unchanged by HF (Supplementary Table S5, Figure S4A) whereas in *Gcn2-null* mice, half of the proteogenic amino acids were elevated by HF, including the branched chain amino acids leucine, isoleucine, and

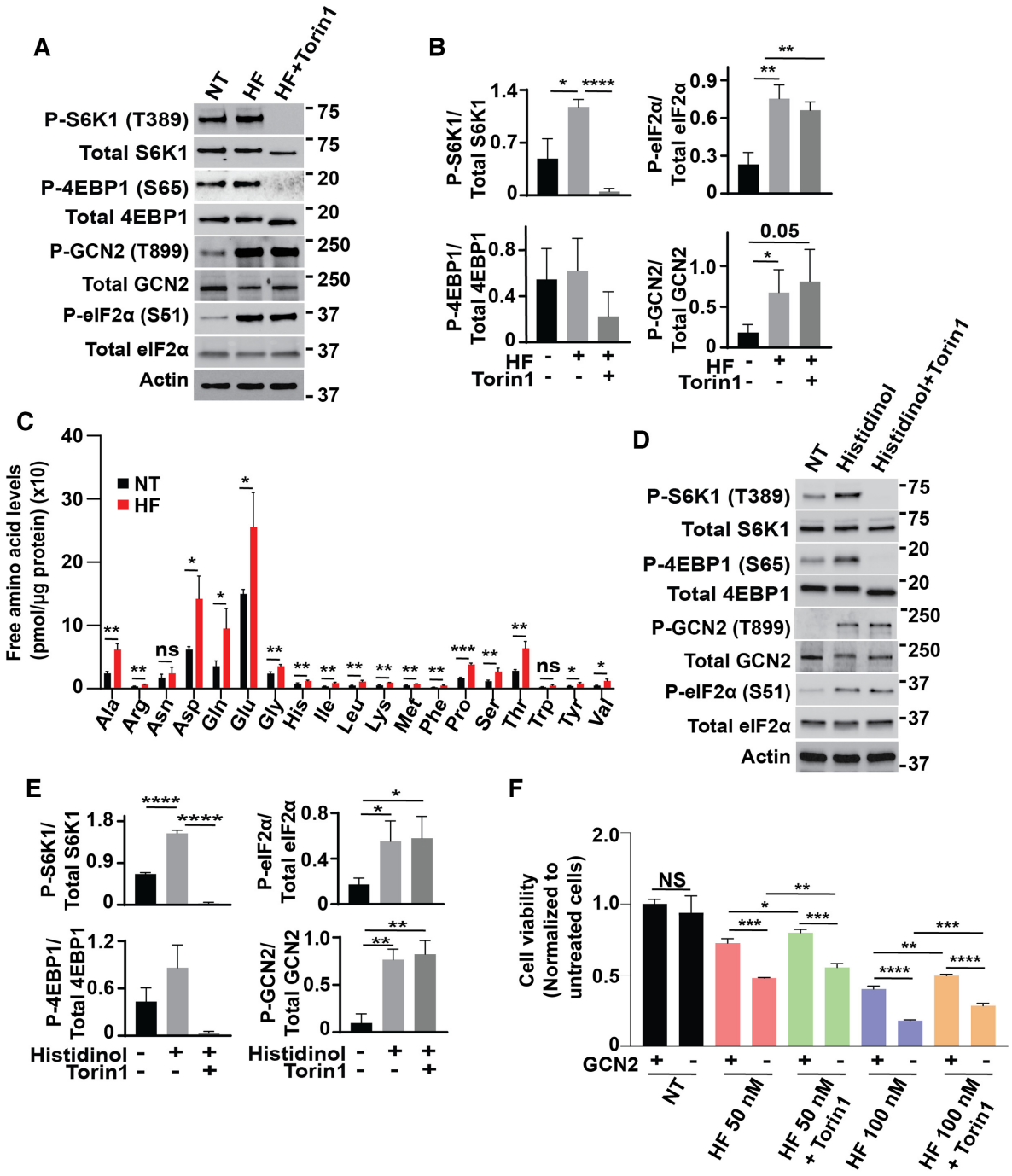

Figure 4. Elevated free amino acids during HF treatment is suggested to enhance mTORC1 signaling. (**A**) MEF cells were treated with 100 nM HF for 6 h in presence or absence of 25 nM Torin1 or left untreated (NT), followed by immunoblot analyses with the indicated antibodies. (**B**) The bar graph shows the changes in the levels of phosphorylated GCN2, eIF2α, S6K1, and 4EBP1. Results were derived from 3 independent experiments, with error bars represented as the means ± SD. Significant differences between treatment groups are indicated: $*P < 0.05$; $**P < 0.005$; $****P < 0.0001$. (**C**) MEF cells were treated with 100 nM HF for 6 h or left untreated (NT), followed by lysis and free amino acids were measured and illustrated in the bar graph. The data was derived from 3 independent experiments, with error bars represented as the means ± SD. Significant differences between treatment groups are indicated: $*P < 0.05$; $**P < 0.005$; $***P < 0.0005$. (**D**) MEF cells were treated with 2 mM histidinol for 6 h in presence or absence of 25 nM Torin1 or left untreated (NT), followed by immunoblot analyses with the indicated antibodies. (**E**) The bar graph shows the changes in the levels of phosphorylated GCN2, eIF2α, S6K1 and 4EBP1. The data was derived from three independent experiments, with error bars represented as the means ± SD. Significant differences between treatment groups are indicated: $*P < 0.05$; $**P < 0.005$; $****P < 0.0001$. (**F**) WT and *Gcn2*$^{-/-}$ MEF cells were treated with either 50 or 100 nM HF for 6 h in presence or absence of 25 nM Torin1 or left untreated (NT), as indicated. Fresh media was then applied to cells for 18 h for a total of 24 h. Cell viability was monitored by the MTT assay. The data was derived from three independent experiments, with error bars represented as the means ± SD. Significant differences between treatment groups are indicated: $*P < 0.05$; $**P < 0.005$; $***P < 0.0005$; $****P < 0.0001$.

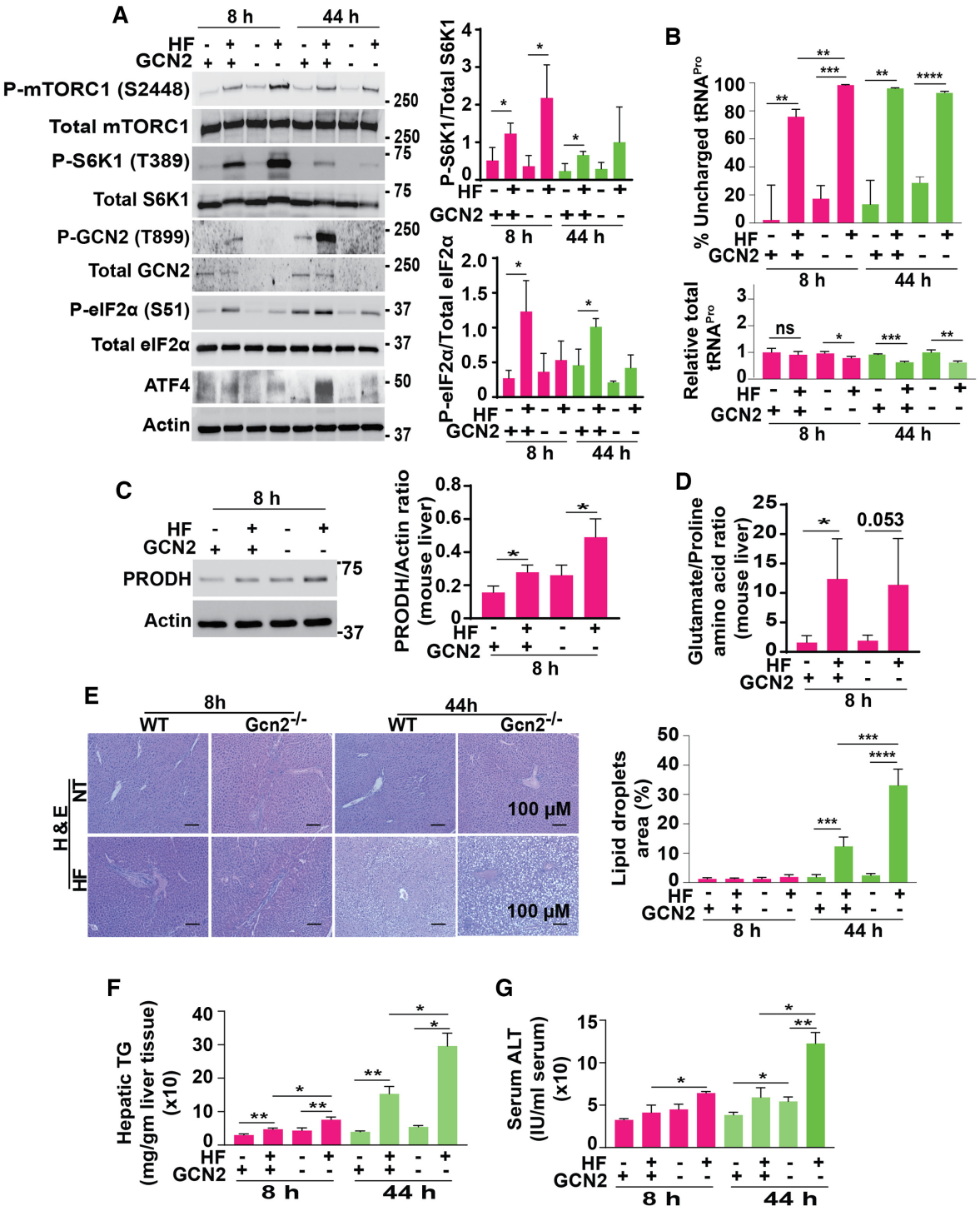

Figure 5. The ISR and mTORC1 are active in livers of mice treated with HF. WT and whole body *Gcn2*$^{-/-}$ mice were injected with HF (0.5 mg/kg) or 0.5% DMSO vehicle. Following 8 h, one group of mice were sacrificed and liver tissues were measured for ISR and mTORC1 signaling, charging of tRNA^{Pro}, and histological analyses. Additionally, another group of mice received a second injection of HF at 24 hours and were sacrificed after 44 h for liver analyses. (**A**) The indicated proteins were measured by immunoblot analyses with specific antibodies. Bar graphs to the right of the immunoblot panels show quantification of phosphorylated S6K1 and eIF2α from three biological replicates. The bar graphs are represented as the means ± SD and $^{*}P < 0.05$. (**B**) Measurements of the percent uncharged tRNA^{Pro} (top panel) and relative total tRNA^{Pro} (bottom panel) by RT-qPCR. Significant differences between treatments are indicated. $^{*}P < 0.05$; $^{**}P < 0.005$; $^{***}P < 0.0005$; $^{****}P < 0.0001$. (**C**) Left panel: hepatic PRODH expression was measured by immunoblot analyses with indicated antibodies; right panel: quantification of hepatic PRODH expression. (**D**) The ratio of hepatic glutamate to proline amino acid was measured. (**E**) Representative images of H&E staining of hepatic tissue for lipid droplets accumulation. Images were captured using light microscopy (100× magnification) (left panel). Quantitation is featured in the accompanying bar graph (right panel). Significant differences between treatments are indicated. $^{***}P < 0.0008$; $^{****}P < 0.0001$. (**F**) Hepatic tissue levels of TG were measured in lipid extracts. (**G**) Liver ALT levels were measured in the serum samples. Bar graphs are represented as the means ± SD, and significant differences between treatments are indicated: $^{*}P < 0.05$; $^{**}P < 0.005$.

valine. Higher levels of BCAA in the circulation may reflect tissue protein breakdown, especially from skeletal muscle which contains high levels of the branched chain amino acids, and in states of nutrient starvation a dominant amino acid flux is from skeletal muscle to liver (59).

HF significantly enhanced the amounts of uncharged $tRNA^{Pro}$ independent of GCN2 function (Figure 5B. upper panel). Levels of total $tRNA^{Pro}$ level were modestly reduced in livers from *Gcn2-null* mice exposed to HF for 8 h and in both WT and *Gcn2*-deleted tissues at 44 h of HF treatment (Figure 5B). There was no significant change in uncharged $tRNA^{Asn}$ levels in response to HF (Supplementary Figure S4C). Since HF increased intracellular free proline levels in MEF cells, we expected liver intracellular free proline concentrations to rise following HF administration in mice. It is noteworthy that liver intracellular free proline concentrations decreased in all mice administered HF (Supplementary Table S6). We also noticed a concomitant increase in liver intracellular free glutamate in these same mice (Supplementary Table S6). It is already reported that in response to nutrient starvation proline can be converted to glutamate (60,61); therefore, we next considered conversion of proline to glutamate following HF exposure. Proline dehydrogenase (POX/PRODH), the enzyme responsible for proline oxidation and glutamate synthesis from proline (60), was significantly increased in the livers of all mice injected with HF but was even higher in the livers of $Gcn2^{-/-}$ mice injected once with HF (Figure 5C). Assessment of the glutamate to proline amino acid ratio in liver with the hepatic PRODH levels indicated a positive relationship between these two measurements (Figure 5D). Collectively, these data support the idea that in parallel to reduced $tRNA^{Pro}$ charging in liver, HF promotes hepatic metabolism of proline to glutamate. These results show *in vivo* that HF lowers charging of $tRNA^{Pro}$, inducing GCN2 and the ISR accompanied by active mTORC1 signaling.

GCN2 protects hepatic tissue during HF exposure

We next addressed the protective functions of hepatic GCN2 in mice administered HF. Loss of G*cn*2 provoked premature morbidity to HF, ending the experimental time line earlier (24–44 h) than originally planned (72 h). Representative haemotoxylin and eosin staining of fixed liver tissues displayed significant induction of steatosis in *Gcn2-null* mice exposed to HF for 44 h as visualized by over 2-fold accumulation of lipid droplets compared to WT tissues (Figure 5E). Levels of hepatic triglycerides were also enhanced in the livers of *Gcn2-null* mice exposed to HF (Figure 5F). Serum ALT level, a marker of hepatic tissue damage, was also elevated to a greater extent in *Gcn2-null* mice administered HF (Figure 5G).

To further evaluate the role of GCN2 in liver during HF exposure, we performed TUNEL assays to assess DNA damage. Our results showed DNA fragmentation predominantly in *Gcn2-null* mice exposed to HF for 44 h (Figure 6A). Cleaved caspase-3 viewed by immunohistochemistry (IHC) was also detected around the hepatic vein areas (especially zone 3) in *Gcn2-null* mice exposed to HF for 8 h, with further enhancement after 44 h of HF exposure (Figure 6B). Necroptosis was also suggested to be enhanced at 44h in livers from *Gcn2-null* mice administered HF, with increased phosphorylation of mixed lineage kinase domain like pseudokinase (MLKL) as visualized by IHC in the *Gcn2*-deficient liver tissues as compared to WT (Figure 6C). Finally, we measured the generation of oxidative stress in the liver in response to HF. Levels of the oxidative stress marker, 4-hydroxynonenal (4-HNE), which is largely attributed to lipid peroxidation and reactive oxygen species (62–64), was significantly increased by HF in both WT and *Gcn2-null* livers, but was exacerbated in livers from *Gcn2-null mice* (Supplementary Figure S5A). Hydrogen peroxide (H_2O_2) levels, a measure of ROS generation, were also increased in both WT and *Gcn2-null* livers (Supplementary Figure S5C). Generation of free radicals, such as ROS and nitric oxide (NO), contribute to hepatic tissue oxidation (65–67). IHC analyses for nitrotryptophan, a molecule associated with NO generation (68), indicated that HF caused massive production of NO in WT livers, with further increased levels in *Gcn2*-deficient livers at 44 h (Supplementary Figure S5B). These results were further supported by hepatic NO levels that were significantly higher in *Gcn2-null* mice exposed to HF as compared to WT counterparts (Supplementary Figure S5D). These results suggest that HF promotes hepatic cell death through production of NO free radicals and GCN2 signaling provides broad protection from these HF insults.

DISCUSSION

Deprivation of many different amino acids potently activates GCN2 eIF2α kinase and the ISR, whereas depletion of certain amino acids represses mTORC1 signaling. This reciprocal regulation ensures necessary coordination between the two adaptive responses during amino acid starvation to prevent proteostasis collapse: the ISR lowers translation initiation while altering metabolism to regain homeostasis, whereas repressed mTORC1 dampens growth capacity by reducing ribosome biogenesis and cap-dependent translation (18). HF is a potent inhibitor of aminoacylation of $tRNA^{Pro}$, thus mimicking nutrient limitation to induce GCN2 and ISR-directed translational control (Figures 1, 2, 5 and 7). However, unlike *bona fide* amino acid limitations, HF does not repress mTORC1 phosphorylation of its targets, 4EBP1 and S6K1, and allows for continued translation of 5′-TOP mRNAs that provide for protein biogenesis. The simultaneous activation of ISR and mTOR signaling by HF emphasizes the different mechanisms by which GCN2 and mTOR sense nutrient limitation: GCN2 directly senses uncharged tRNAs that accumulate during HF while mTORC1 utilizes a hierarchy of proteins to determine if the availability of amino acids is sufficient for growth (Figure 7). In this way, increased uncharged $tRNA^{Pro}$ during HF treatment provides an appropriate signal of nutrient limitation to GCN2. In contrast, mTORC1 inappropriately senses the increased availability of many free amino acids (Figure 4B, Supplementary Table S5) and remains active upon HF treatment. Both GCN2 and mTORC1 were also active in MEF cells treated with histidinol, which thwarts charging of $tRNA^{His}$, demonstrating that nutrient limitation mimetics that block tRNA charging for different amino

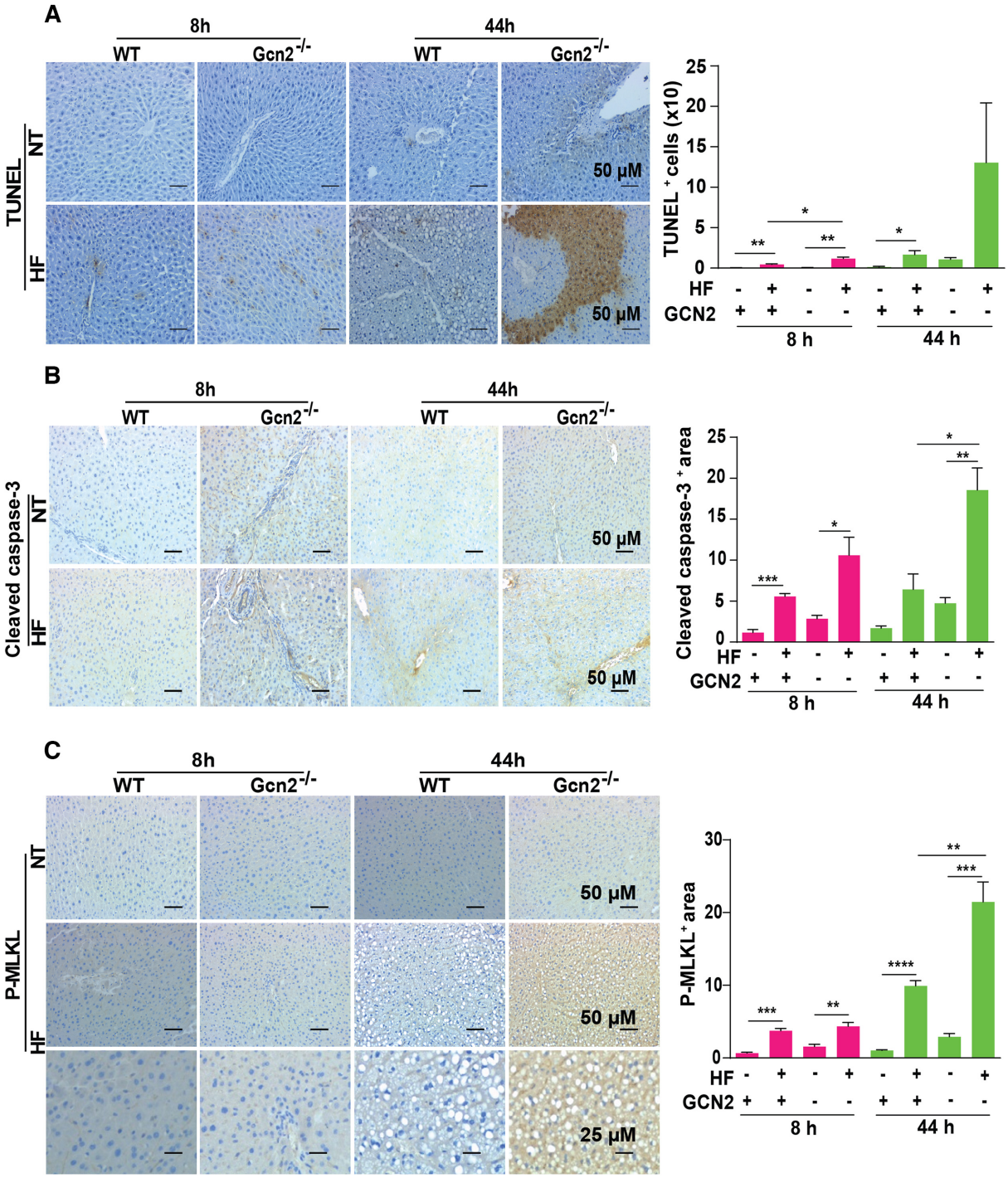

Figure 6. GCN2 protects hepatic tissue during HF treatment. WT and whole body *Gcn2*$^{-/-}$ mice were treated with HF or vehicle for 8 h or 44 h and histological analyses performed to determine the protection functions of GCN2. (**A**) Measurements of the TUNEL assay visualized by light microscopy (200 x magnification) (left panel) and associated quantification is provided in the bar graph (right panel). (**B**) IHC analyses of cleaved caspase-3 obtained by light microscopy (200× magnification) (left panel) and associated quantification is provided in the bar graph (right panel). (**C**) IHC analyses of phosphorylated MLKL obtained by light microscopy (either 200× or 400× magnification) (left panel) and associated quantification is provided in the bar graph (right panel). Significant differences between treatments are indicated. $^{**}P < 0.005$; $^{***}P < 0.0005$; $^{****}P < 0.0001$.

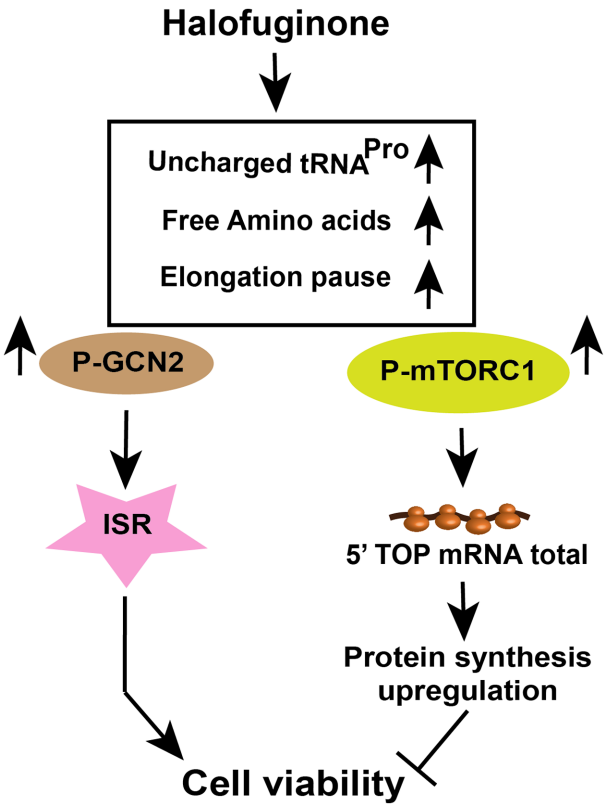

Figure 7. Model for discordant regulation of the GCN2 and mTORC1-directed pathways in response to HF. HF treatment sharply reduces aminoacylation of $tRNA^{Pro}$, which contributes to accumulation of free amino acids and to pausing of elongating ribosomes at proline codons. The HF-triggered events, including accumulating uncharged $tRNA^{Pro}$ activate GCN2, leading to enhanced eIF2α-P and induction of the ISR that enhances cell viability. In parallel, there are high levels of mTORC1 activity, which contributes to enhanced translation of 5′-TOP mRNAs that signal elevated protein biogenesis. Enhanced mTORC1 signaling serves to reduce cell viability in response to HF.

acids trigger discordant regulation of GCN2 and mTORC1 signaling (Figure 4).

A previous report by Averous et al. (69) indicated that histidinol treatment elicits inappropriate regulation of the ISR and the mTORC1, with observed induction of P-eIF2α accompanied by phosphorylation of S6K1. We confirmed these observations and showed histidinol lowered the charging of $tRNA^{His}$ accompanied by enhanced free amino acids, supporting the idea that the different sensing mechanisms of GCN2 and mTORC1 contribute to their different responses to histidinol (Figure 4C and D). Earlier reports also suggested that there are mechanisms in place to ensure appropriate reciprocal regulation between GCN2 and mTORC1 during starvation for certain amino acids (24,25,70,71). For example, mTORC1 repression is not appropriately invoked in *Gcn2-null* mice fed a diet devoid of leucine (24). As illustrated in our study, it is important to emphasize that activation of GCN2 alone is not sufficient to inhibit mTORC1 inhibition, rather GCN2 functions in conjunction with other mechanisms that sense depletion of free amino acids. The mechanisms by which activated GCN2 contributes to mTORC1 inhibition are not yet clear. It is suggested that GCN2 induction of ATF4 can repress mTORC1 through enhanced transcriptional expression of *Redd1* and *Sestrin2*, and downstream of mTORC1 via increased 4EBP1 expression (70,72–75). However, GCN2 has been reported to contribute to repression of mTORC1 during short-term limitations for amino acids via mechanisms that are independent of ATF4 (42,69). These ATF4- independent mechanisms are suggested to involve post-transcriptional control mechanisms involving other target genes that are not yet identified. Finally, it is suggested that activation of GCN2 during lysine deprivation is not critical for repression of mTORC1, suggesting that mechanisms ensuring appropriate reciprocal regulation between GCN2 and mTORC1 may vary depending on which amino acid is limiting (69).

Discordant regulation of GCN2 and mTORC1 can adversely affect cell viability

Discordant regulation of GCN2 and mTORC1 is deleterious to cell adaptation and survival in cells and mice exposed to HF (Figure 7) because synchronous activation of both signal transduction pathways creates a mismatch in the proteostasis network. This premise was supported by our analysis of mice lacking functional GCN2, which showed premature morbidity during HF. Loss of *Gcn2* also greatly exacerbates accumulation of lipid droplets, escalates ROS production and increases hepatic cell death during HF exposure (Figure 6). The idea that mTORC1 activation during amino acid stress makes the organism more vulnerable to damage and death is also supported by improved cell viability following pharmacological inhibition of mTORC1 (Figure 4). These results show that GCN2 is central for adaptive responses to HF-directed stress.

Biomedical implications of discordant regulation of the ISR and mTORC1 pathways

Discordant regulation of the ISR and mTORC1 signaling has been reported in tumors with certain genetic changes. For example, loss of tuberous sclerosis complex leads to constitutive activation of mTORC1 and sharply increased synthesis of proteins that can translocated into the ER and exceed the processing capacity of the organelle (26). The ensuing ER stress induces the unfolded protein response (UPR) that features eIF2α kinase PERK. Activation of the UPR by disruption of TSC function sensitizes the cells to ER stress-induced apoptosis and serves to disrupt proper signaling and metabolic processes directed by insulin (26).

Uncontrolled protein synthesis has also been linked to the ISR activation in the context of proto-oncogene c-MYC (MYC) overexpression. A recent report showed that induced c-MYC in tumor cells substantially enhances protein synthesis, which transiently diminishes free amino acids that triggers activation of GCN2 (76). Induced MYC is intimately linked with activated mTORC1 in heightened ribosome biogenesis and translation. Depletion of GCN2, PERK, or ATF4 resulted in increased apoptosis upon c-MYC activation, emphasizing that activation of ISR provides resistance to MYC induced intrinsic cellular stresses (76).

ISR preconditioning provides therapeutic resistance to stress

Induction of P-eIF2α and the ISR can induce cytoprotective gene expression that provides tissues protection from subsequent stress insults (77). With an eye towards applying the stress-resistant preconditioned state, Peng et al (78) reported that HF treatment could mimic short-term diets lacking proline for increased resistance to surgical stress in mouse models. Preconditioning with HF or dietary restriction prior to surgery that inflicted renal or hepatic ischemic injury afforded tissue protection, including lowered inflammation and preserved organ functions. It was reasoned that nutrient stress prior to surgery triggered cell stress responses, including the ISR, would elicit adaptive gene expression that serve to stabilize proteostasis during a subsequent surgical stress (78). We show here that unlike amino acid starvation, HF does not deplete cellular amino acid levels, rather it increases the free amino acid pool coincident with mTORC1 activation. Since simultaneous activation of the ISR and mTOR pathway is detrimental to cells, we suggest that the beneficial effect of preconditioning by HF is from the activation of the ISR and not the mTORC1 signaling. Moreover, Peng et al (78) used a HF dose of 0.2 mg/kg body weight, whereas 0.5 mg/kg body weight was used in this study; therefore, it is likely that at lower concentration the beneficial effect of HF-induced GCN2-ISR signaling overwhelms potential negative consequences of simultaneous mTORC1 activation. In the absence of GCN2, mTORC1 activation becomes even more prominent (Figure 5A) and mice lacking functional GCN2 became more vulnerable to HF treatment (Figure 6), emphasizing the significance of the GCN2-mediated adaptive response.

DATA AVAILABILITY

All data sets from this study are available in the NCBI GEO database (accession no. - GSE156850).

SUPPLEMENTARY DATA

Supplementary Data are available at NAR Online.

ACKNOWLEDGEMENTS

We thank the members of the Wek and Anthony laboratories for their helpful discussions.

FUNDING

National Institutes of Health [R01DK109714 to T.G.A., R.C.W., R01GM049164, R35GM136331 to R.C.W.]; American Heart Association postdoctoral fellowship (to M.J.H.). Funding for open access charge: NIH.

Conflict of interest statement. R.C.W. has received grant support from Eli Lilly and Company and R.C.W. and T.G.A. serve as scientific advisors to HiberCell; other authors declare no conflicts of interest.

REFERENCES

1. Wek,R.C. (2018) Role of eIF2α kinases in translational control and adaptation to cellular stress. *Cold Spring Harb. Perspect. Biol.*, **10**, pii: a032870.
2. Vattem,K.M. and Wek,R.C. (2004) Reinitiation involving upstream ORFs regulates ATF4 mRNA translation in mammalian cells. *Proc. Natl. Acad. Sci. U.S.A.*, **101**, 11269–11274.
3. Lu,P.D., Harding,H.P. and Ron,D. (2004) Translation reinitiation at alternative open reading frames regulates gene expression in an integrated stress response. *J. Cell Biol.*, **167**, 27–33.
4. Harding,H.P., Novoa,I., Zhang,Y., Zeng,H., Wek,R., Schapira,M. and Ron,D. (2000) Regulated translation initiation controls stress-induced gene expression in mammalian cells. *Mol. Cell*, **6**, 1099–1108.
5. Young,S.K. and Wek,R.C. (2016) Upstream open reading frames differentially regulate gene-specific translation in the integrated stress response. *J. Biol. Chem.*, **291**, 16927–16935.
6. Baird,T.D. and Wek,R.C. (2012) Eukaryotic initiation factor 2 phosphorylation and translational control in metabolism. *Adv. Nutr.*, **3**, 307–321.
7. Hinnebusch,A.G. (2005) Translational regulation of Gcn4 and the general amino acid control of yeast. *Annu. Rev. Microbiol.*, **59**, 407–450.
8. Wu,C.C., Peterson,A., Zinshteyn,B., Regot,S. and Green,R. (2020) Ribosome collisions trigger general stress responses to regulate cell fate. *Cell*, **182**, 404–416.
9. Harding,H.P., Ordonez,A., Allen,F., Parts,L., Inglis,A.J., Williams,R.L. and Ron,D. (2019) The ribosomal P-stalk couples amino acid starvation to GCN2 activation in mammalian cells. *Elife*, **8**, e50149.
10. Inglis,A.J., Masson,G.R., Shao,S., Perisic,O., McLaughlin,S.H., Hegde,R.S. and Williams,R.L. (2019) Activation of GCN2 by the ribosomal P-stalk. *Proc. Natl. Acad. Sci. U.S.A.*, **116**, 4946–4954.
11. Ishimura,R., Nagy,G., Dotu,I., Chuang,J.H. and Ackerman,S.L. (2016) Activation of GCN2 kinase by ribosome stalling links translation elongation with translation initiation. *Elife*, **5**, e14295.
12. Chen,J.J. and Zhang,S. (2019) Heme-regulated eIF2α kinase in erythropoiesis and hemoglobinopathies. *Blood*, **134**, 1697–1707.
13. Guo,X., Aviles,G., Liu,Y., Tian,R., Unger,B.A., Lin,Y.T., Wiita,A.P., Xu,K., Correia,M.A. and Kampmann,M. (2020) Mitochondrial stress is relayed to the cytosol by an OMA1-DELE1-HRI pathway. *Nature*, **579**, 427–432.
14. Fessler,E., Eckl,E.M., Schmitt,S., Mancilla,I.A., Meyer-Bender,M.F., Hanf,M., Philippou-Massier,J., Krebs,S., Zischka,H. and Jae,L.T. (2020) A pathway coordinated by DELE1 relays mitochondrial stress to the cytosol. *Nature*, **579**, 433–437.
15. Walter,P. and Ron,D. (2011) The unfolded protein response: from stress pathway to homeostatic regulation. *Science*, **334**, 1081–1086.
16. Pindel,A. and Sadler,A. (2011) The role of protein kinase R in the interferon response. *J. Interferon Cytokine Res.*, **31**, 59–70.
17. Harding,H.P., Zhang,Y., Zeng,H., Novoa,I., Lu,P.D., Calfon,M., Sadri,N., Yun,C., Popko,B., Paules,R. *et al.* (2003) An integrated stress response regulates amino acid metabolism and resistance to oxidative stress. *Mol. Cell*, **11**, 619–633.
18. Saxton,R.A. and Sabatini,D.M. (2017) mTOR signaling in growth, metabolism, and disease. *Cell*, **168**, 960–976.
19. Roux,P.P. and Topisirovic,I. (2018) Signaling pathways involved in the regulation of mRNA translation. *Mol. Cell. Biol.*, **38**, e00070-18.
20. Jia,J.J., Lahr,R.M., Solgaard,M.T., Moraes,B.J., Pointet,R., Yang,A.D., Celucci,G., Graber,T.E., Hoang,H.D., Niklaus,M.R. *et al.* (2021) mTORC1 promotes TOP mRNA translation through site-specific phosphorylation of LARP1. *Nucleic Acids Res.*, **49**, 3461–3489.
21. Smith,E.M., Benbahouche,N.E.H., Morris,K., Wilczynska,A., Gillen,S., Schmidt,T., Meijer,H.A., Jukes-Jones,R., Cain,K., Jones,C. *et al.* (2021) The mTOR regulated RNA-binding protein LARP1 requires PABPC1 for guided mRNA interaction. *Nucleic Acids Res.*, **49**, 458–478.
22. Meyuhas,O. and Kahan,T. (2015) The race to decipher the top secrets of TOP mRNAs. *Biochim. Biophys. Acta*, **1849**, 801–811.
23. Wolfson,R.L. and Sabatini,D.M. (2017) The dawn of the age of amino acid sensors for the mTORC1 pathway. *Cell Metab.*, **26**, 301–309.
24. Anthony,T.G., McDaniel,B.J., Byerley,R.L., McGrath,B.C., Cavener,D.R., McNurlan,M.A. and Wek,R.C. (2004) Preservation of liver protein synthesis during dietary leucine deprivation occurs at the expense of skeletal muscle mass in mice deleted for eIF2 kinase GCN2. *J. Biol. Chem.*, **279**, 36553–36561.

25. Bunpo,P., Dudley,A., Cundiff,J.K., Cavener,D.R., Wek,R.C. and Anthony,T.G. (2009) GCN2 protein kinase is required to activate amino acid deprivation responses in mice treated with the anti-cancer agent L-asparaginase. *J. Biol. Chem.*, **284**, 32742–32749.
26. Ozcan,U., Ozcan,L., Yilmaz,E., Duvel,K., Sahin,M., Manning,B.D. and Hotamisligil,G.S. (2008) Loss of the tuberous sclerosis complex tumor suppressors triggers the unfolded protein response to regulate insulin signaling and apoptosis. *Mol. Cell*, **29**, 541–551.
27. Keller,T.L., Zocco,D., Sundrud,M.S., Hendrick,M., Edenius,M., Yum,J., Kim,Y.J., Lee,H.K., Cortese,J.F., Wirth,D.F. *et al.* (2012) Halofuginone and other febrifugine derivatives inhibit prolyl-tRNA synthetase. *Nat. Chem. Biol.*, **8**, 311–317.
28. Jiang,H.Y., Wek,S.A., McGrath,B.C., Scheuner,D., Kaufman,R.J., Cavener,D.R. and Wek,R.C. (2003) Phosphorylation of the α subunit of eukaryotic initiation factor 2 is required for activation of NF-κB in response to diverse cellular stresses. *Mol. Cell. Biol.*, **23**, 5651–5663.
29. Willy,J.A., Young,S.K., Stevens,J.L., Masuoka,H.C. and Wek,R.C. (2015) CHOP links endoplasmic reticulum stress to NF-κB activation in the pathogenesis of nonalcoholic steatohepatitis. *Mol. Biol. Cell*, **26**, 2190–2204.
30. Fusakio,M.E., Willy,J.A., Wang,Y., Mirek,E.T., Al Baghdadi,R.J., Adams,C.M., Anthony,T.G. and Wek,R.C. (2016) Transcription factor ATF4 directs basal and stress-induced gene expression in the unfolded protein response and cholesterol metabolism in the liver. *Mol. Biol. Cell*, **27**, 1536–1551.
31. Jiang,J., Srivastava,S., Seim,G., Pavlova,N.N., King,B., Zou,L., Zhang,C., Zhong,M., Feng,H., Kapur,R. *et al.* (2019) Promoter demethylation of the asparagine synthetase gene is required for an ATF4-dependent adaptation to asparagine depletion. *J. Biol. Chem.*, **294**, 18674–18684.
32. Evans,M.E., Clark,W.C., Zheng,G. and Pan,T. (2017) Determination of tRNA aminoacylation levels by high-throughput sequencing. *Nucleic Acids Res.*, **45**, e133.
33. Teske,B.F., Baird,T.D. and Wek,R.C. (2011) Methods for analyzing eIF2 kinases and translational control in the unfolded protein response. *Methods Enzymol.*, **490**, 333–356.
34. McGlincy,N.J. and Ingolia,N.T. (2017) Transcriptome-wide measurement of translation by ribosome profiling. *Methods*, **126**, 112–129.
35. Langmead,B., Trapnell,C., Pop,M. and Salzberg,S.L. (2009) Ultrafast and memory-efficient alignment of short DNA sequences to the human genome. *Genome Biol.*, **10**, R25.
36. Kim,D., Langmead,B. and Salzberg,S.L. (2015) HISAT: a fast spliced aligner with low memory requirements. *Nat. Methods*, **12**, 357–360.
37. Anders,S., Pyl,P.T. and Huber,W. (2015) HTSeq-a Python framework to work with high-throughput sequencing data. *Bioinformatics*, **31**, 166–169.
38. Love,M.I., Huber,W. and Anders,S. (2014) Moderated estimation of fold change and dispersion for RNA-seq data with DESeq2. *Genome Biol.*, **15**, 550.
39. Li,W., Wang,W., Uren,P.J., Penalva,L.O.F. and Smith,A.D. (2017) Riborex: fast and flexible identification of differential translation from Ribo-seq data. *Bioinformatics*, **33**, 1735–1737.
40. Young,M.D., Wakefield,M.J., Smyth,G.K. and Oshlack,A. (2010) Gene ontology analysis for RNA-seq: accounting for selection bias. *Genome Biol.*, **11**, R14.
41. Kramer,A., Green,J., Pollard,J. Jr and Tugendreich,S. (2014) Causal analysis approaches in Ingenuity Pathway Analysis. *Bioinformatics*, **30**, 523–530.
42. Nikonorova,I.A., Mirek,E.T., Signore,C.C., Goudie,M.P., Wek,R.C. and Anthony,T.G. (2018) Time-resolved analysis of amino acid stress identifies eIF2 phosphorylation as necessary to inhibit mTORC1 activity in liver. *J. Biol. Chem.*, **293**, 5005–5015.
43. Kim,H.G., Huang,M., Xin,Y., Zhang,Y., Zhang,X., Wang,G., Liu,S., Wan,J., Ahmadi,A.R., Sun,Z. *et al.* (2019) The epigenetic regulator SIRT6 protects the liver from alcohol-induced tissue injury by reducing oxidative stress in mice. *J. Hepatol.*, **71**, 960–969.
44. Brunt,E.M. (2001) Nonalcoholic steatohepatitis: definition and pathology. *Semin. Liver Dis.*, **21**, 3–16.
45. Kleiner,D.E., Brunt,E.M., Van Natta,M., Behling,C., Contos,M.J., Cummings,O.W., Ferrell,L.D., Liu,Y.C., Torbenson,M.S., Unalp-Arida,A. *et al.* (2005) Design and validation of a histological scoring system for nonalcoholic fatty liver disease. *Hepatology*, **41**, 1313–1321.
46. Fawcett,T.W., Martindale,J.L., Guyton,K.Z., Hai,T. and Holbrook,N.J. (1999) Complexes containing activating transcription factor (ATF)/cAMP-responsive-element-binding protein (CREB) interact with the CCAAT/enhancer-binding protein (C/EBP)-ATF composite site to regulate Gadd153 expression during the stress response. *Biochem. J.*, **339**, 135–141.
47. Young,S.K., Palam,L.R., Wu,C., Sachs,M.S. and Wek,R.C. (2016) Ribosome elongation stall directs gene-specific translation in the integrated stress response. *J. Biol. Chem.*, **291**, 6546–6558.
48. Young,S.K., Willy,J.A., Wu,C., Sachs,M.S. and Wek,R.C. (2015) Ribosome reinitiation directs gene-specific translation and regulates the integrated stress response. *J. Biol. Chem.*, **290**, 28257–28271.
49. Palam,L.R., Baird,T.D. and Wek,R.C. (2011) Phosphorylation of eIF2 facilitates ribosomal bypass of an inhibitory upstream ORF to enhance CHOP translation. *J. Biol. Chem.*, **286**, 10939–10949.
50. Lee,Y.Y., Cevallos,R.C. and Jan,E. (2009) An upstream open reading frame regulates translation of GADD34 during cellular stresses that induce eIF2α phosphorylation. *J. Biol. Chem.*, **284**, 6661–6673.
51. Thoreen,C.C., Chantranupong,L., Keys,H.R., Wang,T., Gray,N.S. and Sabatini,D.M. (2012) A unifying model for mTORC1-mediated regulation of mRNA translation. *Nature*, **485**, 109–113.
52. Yamashita,R., Suzuki,Y., Takeuchi,N., Wakaguri,H., Ueda,T., Sugano,S. and Nakai,K. (2008) Comprehensive detection of human terminal oligo-pyrimidine (TOP) genes and analysis of their characteristics. *Nucleic Acids Res.*, **36**, 3707–3715.
53. Thoreen,C.C., Kang,S.A., Chang,J.W., Liu,Q., Zhang,J., Gao,Y., Reichling,L.J., Sim,T., Sabatini,D.M. and Gray,N.S. (2009) An ATP-competitive mammalian target of rapamycin inhibitor reveals rapamycin-resistant functions of mTORC1. *J. Biol. Chem.*, **284**, 8023–8032.
54. Manifava,M., Smith,M., Rotondo,S., Walker,S., Niewczas,I., Zoncu,R., Clark,J. and Ktistakis,N.T. (2016) Dynamics of mTORC1 activation in response to amino acids. *Elife*, **5**, pii: e19960.
55. Bertolo,R.F. and Burrin,D.G. (2008) Comparative aspects of tissue glutamine and proline metabolism. *J. Nutr.*, **138**, 2032S–2039S.
56. Hansen,B.S., Vaughan,M.H. and Wang,L. (1972) Reversible inhibition by histidinol of protein synthesis in human cells at the activation of histidine. *J. Biol. Chem.*, **247**, 3854–3857.
57. Wanders,D., Stone,K.P., Forney,L.A., Cortez,C.C., Dille,K.N., Simon,J., Xu,M., Hotard,E.C., Nikonorova,I.A., Pettit,A.P. *et al.* (2016) Role of GCN2-independent signaling through a noncanonical PERK/NRF2 pathway in the physiological responses to dietary methionine restriction. *Diabetes*, **65**, 1499–1510.
58. Nikonorova,I.A., Al-Baghdadi,R.J.T., Mirek,E.T., Wang,Y., Goudie,M.P., Wetstein,B.B., Dixon,J.L., Hine,C., Mitchell,J.R., Adams,C.M. *et al.* (2017) Obesity challenges the hepatoprotective function of the integrated stress response to asparaginase exposure in mice. *J. Biol. Chem.*, **292**, 6786–6798.
59. Brosnan,J.T. (2003) Interorgan amino acid transport and its regulation. *J. Nutr.*, **133**, 2068S–2072S.
60. Phang,J.M. (2019) Proline metabolism in cell regulation and cancer biology: recent advances and hypotheses. *Antioxid. Redox. Signal.*, **30**, 635–649.
61. Liu,W., Le,A., Hancock,C., Lane,A.N., Dang,C.V., Fan,T.W. and Phang,J.M. (2012) Reprogramming of proline and glutamine metabolism contributes to the proliferative and metabolic responses regulated by oncogenic transcription factor c-MYC. *Proc. Natl. Acad. Sci. U.S.A.*, **109**, 8983–8988.
62. Breitzig,M., Bhimineni,C., Lockey,R. and Kolliputi,N. (2016) 4-Hydroxy-2-nonenal: a critical target in oxidative stress? *Am. J. Physiol. Cell Physiol.*, **311**, C537–C543.
63. Ayala,A., Munoz,M.F. and Arguelles,S. (2014) Lipid peroxidation: production, metabolism, and signaling mechanisms of malondialdehyde and 4-hydroxy-2-nonenal. *Oxid. Med. Cell Longev.*, **2014**, 360438.
64. Benedetti,A., Comporti,M. and Esterbauer,H. (1980) Identification of 4-hydroxynonenal as a cytotoxic product originating from the peroxidation of liver microsomal lipids. *Biochim. Biophys. Acta*, **620**, 281–296.
65. Cichoż-Lach,H. and Michalak,A. (2014) Oxidative stress as a crucial factor in liver diseases. *World J. Gastroenterol.*, **20**, 8082–8091.
66. Li,S., Tan,H.Y., Wang,N., Zhang,Z.J., Lao,L., Wong,C.W. and Feng,Y. (2015) The role of oxidative stress and antioxidants in liver diseases. *Int. J. Mol. Sci.*, **16**, 26087–26124.

67. Wang,K. (2014) Molecular mechanisms of hepatic apoptosis. *Cell Death. Dis.*, **5**, e996.
68. Nuriel,T., Hansler,A. and Gross,S.S. (2011) Protein nitrotryptophan: formation, significance and identification. *J. Proteomics*, **74**, 2300–2312.
69. Averous,J., Lambert-Langlais,S., Mesclon,F., Carraro,V., Parry,L., Jousse,C., Bruhat,A., Maurin,A.C., Pierre,P., Proud,C.G. *et al.* (2016) GCN2 contributes to mTORC1 inhibition by leucine deprivation through an ATF4 independent mechanism. *Sci. Rep.*, **6**, 27698.
70. Ye,J.B., Palm,W., Peng,M., King,B., Lindsten,T., Li,M.O., Koumenis,C. and Thompson,C.B. (2015) GCN2 sustains mTORC1 suppression upon amino acid deprivation by inducing Sestrin2. *Gene Dev*, **29**, 2331–2336.
71. Yuan,W., Guo,S., Gao,J., Zhong,M., Yan,G., Wu,W., Chao,Y. and Jiang,Y. (2017) General control nonderepressible 2 (GCN2) kinase inhibits target of rapamycin complex 1 in response to amino acid starvation in *Saccharomyces cerevisiae*. *J. Biol. Chem.*, **292**, 2660–2669.
72. Dennis,M.D., McGhee,N.K., Jefferson,L.S. and Kimball,S.R. (2013) Regulated in DNA damage and development 1 (REDD1) promotes cell survival during serum deprivation by sustaining repression of signaling through the mechanistic target of rapamycin in complex 1 (mTORC1). *Cell. Signal.*, **25**, 2709–2716.
73. Xu,D., Dai,W., Kutzler,L., Lacko,H.A., Jefferson,L.S., Dennis,M.D. and Kimball,S.R. (2020) ATF4-mediated upregulation of REDD1 and Sestrin2 Suppresses mTORC1 activity during prolonged leucine deprivation. *J. Nutr.*, **150**, 1022–1030.
74. Yamaguchi,S., Ishihara,H., Yamada,T., Tamura,A., Usui,M., Tominaga,R., Munakata,Y., Satake,C., Katagiri,H., Tashiro,F. *et al.* (2008) ATF4-mediated induction of 4E-BP1 contributes to pancreatic beta cell survival under endoplasmic reticulum stress. *Cell Metab.*, **7**, 269–276.
75. Kang,M.J., Vasudevan,D., Kang,K., Kim,K., Park,J.E., Zhang,N., Zeng,X., Neubert,T.A., Marr,M.T. 2nd and Ryoo,H.D. (2017) 4E-BP is a target of the GCN2-ATF4 pathway during Drosophila development and aging. *J. Cell Biol.*, **216**, 115–129.
76. Tameire,F., Verginadis,I.I., Leli,N.M., Polte,C., Conn,C.S., Ojha,R., Salas Salinas,C., Chinga,F., Monroy,A.M., Fu,W. *et al.* (2019) ATF4 couples MYC-dependent translational activity to bioenergetic demands during tumour progression. *Nat. Cell Biol.*, **21**, 889–899.
77. Lu,P.D., Jousse,C., Marciniak,S.J., Zhang,Y., Novoa,I., Scheuner,D., Kaufman,R.J., Ron,D. and Harding,H.P. (2004) Cytoprotection by pre-emptive conditional phosphorylation of translation initiation factor 2. *EMBO J.*, **23**, 169–179.
78. Peng,W., Robertson,L., Gallinetti,J., Mejia,P., Vose,S., Charlip,A., Chu,T. and Mitchell,J.R. (2012) Surgical stress resistance induced by single amino acid deprivation requires Gcn2 in mice. *Sci. Transl. Med.*, **4**, 118ra111.